Article:

Ducrot, Aurélien B orcid.org/0000-0003-3463-926X, Coulson, Ben A, Perutz, Robin N orcid.org/0000-0001-6286-0282 et al. (1 more author) (2016) Light-Induced Activation of a Molybdenum Oxotransferase Model within a Ru(II)-Mo(VI) Dyad. Inorganic Chemistry. 6b01485. 12583−12594. ISSN 0020-1669

https://doi.org/10.1021/acs.inorgchem.6b01485

Inorganic Chemistry

Article

pubs.acs.org/IC

Light-Induced Activation of a Molybdenum Oxotransferase Model within a Ru(II)−Mo(VI) Dyad

Aurélien B. Ducrot, Ben A. Coulson, Robin N. Perutz, and Anne-Kathrin Duhme-Klair*

Department of Chemistry, University of York, Heslington, York YO10 5DD, United Kingdom

Supporting Information

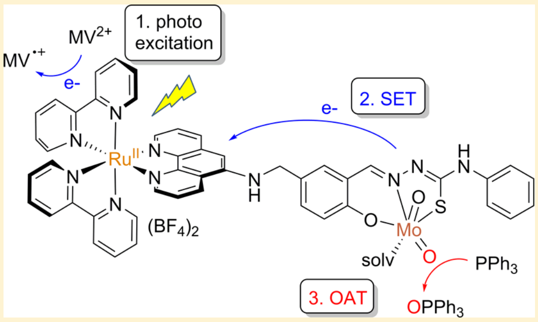

ABSTRACT: Nature uses molybdenum-containing enzymes to catalyze oxygen atom transfer (OAT) from water to organic substrates. In these enzymes, the two electrons that are released during the reaction are rapidly removed, one at a time, by spatially separated electron transfer units. Inspired by this design, a Ru(II)−Mo(VI) dyad was synthesized and characterized, with the aim of accelerating the rate-determining step in the *cis*-dioxo molybdenum-catalyzed OAT cycle, the transfer of an oxo ligand to triphenyl phosphine, via a photo-oxidation process. The dyad consists of a photoactive bis(bipyridyl)-phenanthroline ruthenium moiety that is covalently linked to a bioinspired *cis*-dioxo molybdenum thiosemicarbazone complex. The quantum yield and luminescence lifetimes of the dyad $[Ru(bpy)_2(\mathbf{L^2})MoO_2(solv)]^{2+}$ were determined. The major component of the luminescence decay in MeCN solution (τ = 1149 ± 2 ns, 67%) corresponds closely to the lifetime of excited $[Ru(bpy)_2(phen\text{-}NH_2)]^{2+}$, while the minor component (τ = 320 ± 1 ns, 31%) matches that of $[Ru(bpy)_2(H_2\text{-}\mathbf{L^2})]^{2+}$. In addition, the (spectro)electrochemical properties of the system were investigated. Catalytic tests showed that the dyad-catalyzed OAT from dimethyl sulfoxide to triphenyl phosphine proceeds significantly faster upon irradiation with visible light than in the dark. Methylviologen acts as a mediator in the photoredox cycle, but it is regenerated and hence only required in stoichiometric amounts with respect to the catalyst rather than sacrificial amounts. It is proposed that oxidative quenching of the photoexcited Ru unit, followed by intramolecular electron transfer, leads to the production of a reactive one-electron oxidized catalyst, which is not accessible by electrochemical methods. A significant, but less pronounced, rate enhancement was observed when an analogous bimolecular system was tested, indicating that intramolecular electron transfer between the photosensitizer and the catalytic center is more efficient than intermolecular electron transfer between the separate components.

INTRODUCTION

Metal-containing oxidoreductases play an important role in biological processes by catalyzing selective oxygenations, in particular, those that involve $^3O_2$ activation or oxygen atom transfer (OAT) from water to an organic substrate. To be able to utilize these "green oxygen sources" effectively and under mild conditions, metalloenzymes rely on efficient electron transfer chains that involve spatially separated electron transfer units, such as Fe/S clusters and/or cytochromes to regenerate their active sites (Figure 1, left).[1]

In the search for functional bioinspired catalysts the importance of an overall design that includes electron transfer components and, in particular, proton-coupled electron transfer is increasingly recognized,[3,4] and a number of second-generation model complexes that contain enzyme active-site mimics that are covalently linked to redox-active units have been reported. Electrochemical approaches, for example, have utilized rapid one-electron transfer components, such as ferrocene.[5−7]

These second-generation models represent a significant advancement over conventional molybdoenzyme models that catalyze the thermodynamically favorable OAT reaction from sulfoxides to tertiary phosphines, but they do not have additional redox centers built into their design. In these models, the oxidative and reductive half-reaction take place at the Mo center (Figure 1, right). The catalytic activity of these first-generation models is often limited by slow kinetics due to charge buildup at the Mo center and the formation of inactive Mo(V) dimers as a result of the comproportionation of Mo(IV) and Mo(VI).[8]

In our search for an advanced design, we were inspired by catalytic systems that exploit photoredox processes, since they offer the opportunity of harnessing solar energy. Because of their high quantum yields, long excitation wavelengths, photostability, and long lifetimes, polypyridine complexes of metal cations with d^6 low-spin configuration, such as Ru(II), Re(I), and Ir(III) are frequently used as photoactive units in heterometallic systems to convert light energy to chemical energy. Inspired by photosystem II, manganese model complexes have been linked to $[Ru(bpy)_3]^{2+}$-type photosensitizers to target the four-electron oxidation of H_2O by taking advantage of photoinduced electron transfer (PeT).[9] Similarly, bioinspired dyads that mimic hydrogenases have been

Received: June 23, 2016

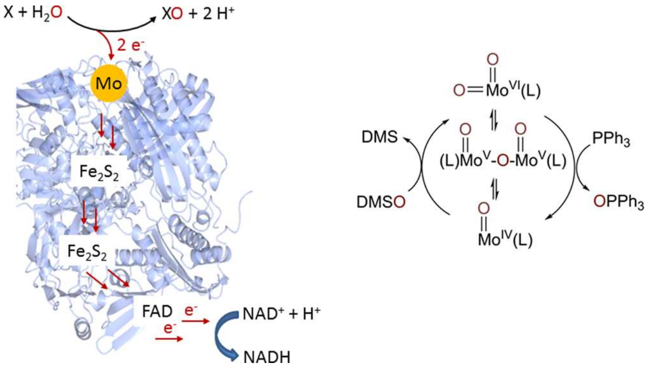

Figure 1. (left) Schematic electron-transfer chain in a metalloenzyme, as exemplified by xanthine dehydrogenase (pdb code 3am9, Mo = molybdenum-containing active site, X = xanthine). (right) Conventional "bioinspired" OAT cycle in which both the oxidative and reductive half-reaction take place at the Mo center of a synthetic model complex (DMSO + Ph$_3$P → DMS + Ph$_3$PO: $\Delta H = -47$ kcal mol^{-1}, gas phase[2]).

studied with the aim of catalyzing the light-driven production of H$_2$.[10,11]

Recently, there has been increasing interest in photoredox catalysis[12−14] and its scope in the photocatalyic oxygenation of organic substrates using clean O atom sources, such as $^3O_2$ or H$_2$O, which is highly desirable on both environmental and economic grounds. For example, Hamelin and Torelli et al. used a Ru(II)−Cu(II) dyad to oxidize sulfides, phosphines, and alkenes photocatalytically with $^3O_2$ as the oxygen atom source and triethanolamine as sacrificial electron donor.[15] Aukauloo, Banse, and Leibl et al., reported a Ru(II)−Fe(II) dyad that allows the photogeneration of a highly reactive oxo-Fe(IV) center from an Fe(II)-coordinated H$_2$O molecule using $[Co(NH_3)_5Cl]^{2+}$ as sacrificial electron acceptor, followed by transfer of the oxygen atom to PPh$_3$.[16] To drive the photoactivated OAT, the two-electron oxidation of the substrate had to be coupled with two rapid proton-coupled electron transfer steps.

Since Mo is chosen by nature as OAT catalyst par excellence based on its ability to redox cycle between oxidation states VI, V, and IV,[17] we are interested in utilizing bioinspired Mo complexes as catalysts in dyads designed to facilitate substrate oxidation via a photoredox process. Enemark and Kirk et al. already demonstrated in an early study that a Mo center can be photoactivated via an antenna-mediated electron transfer process by covalently linking an oxo-Mo(V) unit to porphyrin-Fe(III) or Zn(II) complexes (Scheme 1a).[18,19] Although catalytic investigations were not reported for these dyads, the study highlighted photoactivation as a potential way of initiating intercomponent electron transfer. More recently, Heinze et al. appended two redox-active ferrocene units to a *cis*-dioxo-Mo(VI) complex to mimic the electron-transfer chain in the molybdenum enzyme sulfite oxidase (Scheme 1b).[7] It was observed that chemical oxidation to the diferrocenium dication greatly accelerated OAT to PMe$_3$, consistent with an accelerated attack of the phosphine at the oxo ligand, coupled with intramolecular electron transfer.

Drawing on these precedents, we anticipated that the addition of a photoactivatable electron acceptor to a *cis*-dioxo-Mo(VI) center could promote the attack of a phosphine at the oxo ligand in a similar way, thereby increasing catalytic activity. Of the many synthetic ligand systems that were developed in bioinspired approaches to model the function of the molybdenum enzymes[20−24] we chose thiosemicarbazones, whose synthesis is straightforward and allows a variety of substituents to be incorporated.[25−27] We recently reported the electronic fine-tuning of series of six *cis*-dioxo-Mo(VI) complexes with thiosemicarbazone ligands for OAT and found that electron-withdrawing substituents increase the rate of the OAT to triphenylphosphine, while electron-donating groups have the opposite effect.[28] This observation is consistent with the generally accepted OAT mechanism, which starts with the nucleophilic attack of the phosphine lone pair on a vacant π^* orbital of one of the oxo-ligands, leading to the formation of an oxo-Mo(IV) species and phosphine oxide via a phosphine oxide-coordinated intermediate in the rate-determining step.[29,30] Accordingly, a decrease of the electron density on the *cis*-dioxo-Mo(VI) center renders the oxo ligand more susceptible to attack and lowers the energy of the transition state by ameliorating negative charge buildup, giving rise to faster reaction rates.

Scheme 1. Structures of Bioinspired oxo-Mo Complexes with Appended Electron-Transfer Units

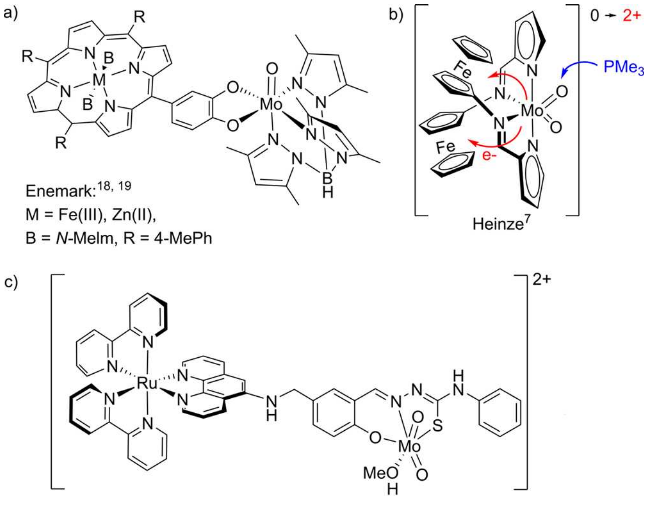

This work: Ru(II)-Mo(VI) dyad: $[Ru(bpy)_2(\mathbf{L^2})MoO_2(MeOH)]^{2+}$

Here, we report the synthesis and the characterization of the Ru(II)−Mo(VI) dyad $[Ru(bpy)_2(\mathbf{L^2})MoO_2(solv)](BF_4)_2$, in which one coordination site on the Mo(VI) center is occupied by a solvent molecule (Scheme 1c). The photoactive bis(bipyridyl)-phenanthroline ruthenium moiety is linked to the Mo-based OAT catalyst by a methylamine group to define the spatial separation while allowing flexibility to facilitate intramolecular electron transfer from the Mo-coordinated thiosemicarbazone ligand to the photo-oxidized Ru^{III}-bpy/phen$^{\bullet-}$-unit. The photophysical, spectroscopic, and electrochemical properties of the dyad and the results of photocatalytic tests are reported.

EXPERIMENTAL SECTION

Materials and Instruments. Ammonium tetrafluoroborate, paraformaldehyde, 1,10-phenanthroline-5-amine, 4-phenylthiosemicarbazide, and sodium molybdate dihydrate were purchased from Aldrich. Acetylacetic acid was purchased from BDH chemicals, ammonium hexafluorophosphate from Alfa Aesar, salicylaldehyde from Fluka, triethylamine from Fisher Chemicals, and *cis*-bis(2,2′-bipyridine)-dichlororuthenium hydrate from Acros organics. $[MoO_2(acac)_2]$[31] and 5-chloromethyl-2-hydroxylbenzaldehyde[32] were synthesized according to reported procedures. Solvents for syntheses were dried and stored

Scheme 2. Synthesis of the Dyad [Ru(bpy)$_2$(L^2)MoO$_2$(MeOH)](BF$_4$)$_2$ and the Structure of [MoO$_2$(L$^{\rm Me}$)MeOH)]

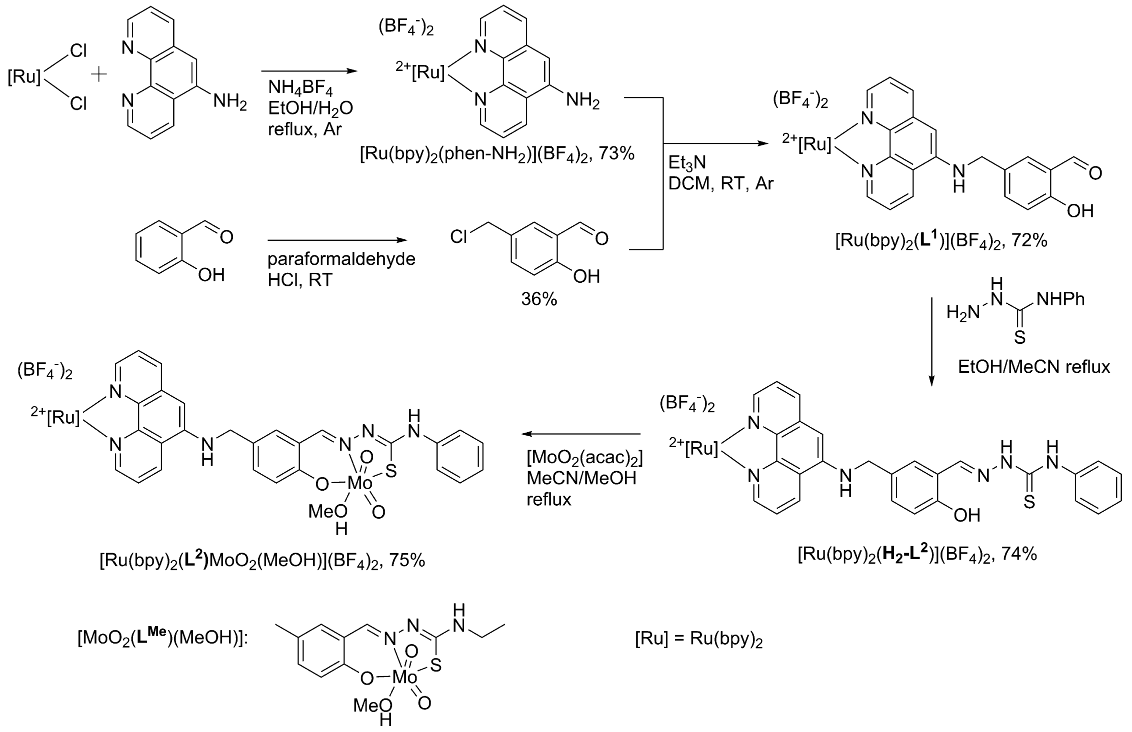

over 3 Å molecular sieves. ^{1}H and ^{13}C{^{1}H} decoupled NMR spectra were recorded on a Jeol ECS400 instrument (^{1}H NMR 400 MHz, ^{13}C NMR 100.6 MHz, ^{19}F 376.5 MHz), a Bruker 500 (^{1}H NMR 500 MHz, ^{13}C NMR 125.8 MHz, ^{31}P 202.5 MHz), and a Bruker 700 (^{1}H NMR 700 MHz, ^{13}C NMR 176.0 MHz). Assignment of resonances was confirmed based on COSY, DEPT135, and HSQC spectra. Decomposition points were measured with a Stuart Scientific SMP3 apparatus. Elemental analyses of compounds were performed with an Exeter CE-440 elemental analyzer. Electron spray ionization mass spectrometry (ESI-MS) and high-resolution mass spectra were recorded with a Bruker microTOF electrospray mass spectrometer, and mass values are quoted for ^{102}Ru and ^{98}Mo. UV−visible absorption spectra were measured using an Agilent 8453 spectrometer. Emission spectra were recorded on a Hitachi F-4500 fluorescence spectrophotometer. Excited-state lifetimes were measured on an Edinburgh Instruments FLS980 fluorescence lifetime instrument.

Synthesis. The synthetic method is shown in Scheme 2.

[Ru(bpy)$_2$(phen-NH$_2$)](BF$_4$)$_2$.[33] *cis*-Bis(2,2′-bipyridine)-dichlororuthenium hydrate (1.06 g, 2.04 mmol) and 1,10-phenanthroline-5-amine (0.465 g, 2.38 mmol) were dissolved in a mixture of ethanol (160 mL) and water (80 mL). The resulting solution was degassed and refluxed under Ar for 20 h. The ethanol was removed under reduced pressure, and a solution of ammonium tetrafluoroborate (2.14 g, 20.4 mmol) in water was added to precipitate the product as tetrafluoroborate salt. The precipitate was isolated by filtration and washed with water. The crude product was purified by column chromatography on alumina (toluene/acetonitrile 1:1). The product was solubilized in a minimum volume of acetonitrile and reprecipitated with diethyl ether. The bright orange precipitate was isolated and dried under vacuum (1.164 g, 73%).

Decomposition point 215 °C.

^{1}H NMR (CD$_3$CN, 500 MHz): δ 8.61 (d, ^{3}J = 8.55 Hz, 1H, C$H_{\rm phen}$), 8.52 (t, ^{3}J = 6.65 Hz, 2H, C$H_{\rm bpy}$), 8.48 (d, ^{3}J = 8.25 Hz, 2H, C$H_{\rm bpy}$), 8.21 (d, ^{3}J = 8.3 Hz, 1H, C$H_{\rm phen}$), 8.10−8.04 (m, 3H, 2 C$H_{\rm bpy}$ + 1C$H_{\rm phen}$), 7.99 (t, ^{3}J = 8 Hz, 2H, C$H_{\rm bpy}$), 7.83 (dd, ^{3}J = 13.6 Hz, ^{3}J = 5.55 Hz, 2H, C$H_{\rm bpy}$), 7.71−7.67 (m, 2H, C$H_{\rm phen}$), 7.55 (dd, ^{3}J = 16.9 Hz, ^{3}J = 5.3 Hz, 2H, C$H_{\rm bpy}$), 7.49 (dd, ^{3}J = 8.4 Hz, ^{3}J = 5.2 Hz, 1H, C$H_{\rm phen}$), 7.43 (m, 2H, C$H_{\rm bpy}$), 7.23 (m, 2H, C$H_{\rm bpy}$), 7.17 (s, 1H, C$H_{\rm phen}$), 5.57 (s, 2H, NH).

^{13}C NMR (CD$_3$CN, 125.8 MHz): δ 158.3, 158.0, 153.14, 152.97, 152.88, 152.81, 149.3, 148.5, 145.5, 142.9, 138.7, 138.6, 134.7, 133.9, 132.5, 128.48, 128.44, 128.35, 126.8, 125.7, 125.20, 125.15, 125.11, 125.0, 104.4.

^{19}F NMR (CD$_3$CN, 376.5 MHz): δ −151.6.

MS-ESI: *m*/*z* 304.5595, [M^{2+}] calcd. for C$_{32}$H$_{25}$N$_7$Ru 304.5606.

C$_{32}$H$_{25}$B$_2$F$_8$ N$_7$Ru + 1.5 H$_2$O: Anal. Calcd C 47.49, H 3.49, N 12.12; found C 47.56, H 3.22, N 12.00.

[Ru(bpy)$_2$(L^1)](BF$_4$)$_2$. [Ru(bpy)$_2$(phen-NH$_2$)](BF$_4$)$_2$ (1.11 g, 1.42 mmol) was suspended in a solution of 5-chloromethyl-2-hydroxybenzaldehyde (0.29 g, 1.70 mmol) in dichloromethane (30 mL) under an argon atmosphere. Triethylamine (600 μL, 4.33 mmol) was added dropwise, and the resultant mixture was stirred overnight. Ammonium tetrafluoroborate (0.45 g, 4.29 mmol) was added, and the mixture was stirred vigorously for 5 min prior to washing with water. The organic layer was dried over magnesium sulfate and concentrated to dryness. The product was triturated with diethyl ether to yield a red solid (1 g, 72%).

Decomposition point 283 °C.

^{1}H NMR (CD$_3$CN, 400 MHz): δ 9.93 (s, 1H, CHO), 8.72 (d, ^{3}J = 8.56 Hz, 1H, C$H_{\rm phen}$), 8.54−8.47 (m, 4H, C$H_{\rm bpy}$), 8.16 (d, ^{3}J = 8.36 Hz, 1H, C$H_{\rm phen}$), 8.11−8.04 (m, 3 C$H_{\rm bpy}$ + 1C$H_{\rm phen}$), 7.99 (t, ^{3}J = 7.8 Hz, 2H, C$H_{\rm bpy}$), 7.85−7.80 (m, 3H, 2 C$H_{\rm bpy}$ + 1C$H_{\rm Ar}$), 7.71 (dd, ^{3}J = 8.6 Hz, ^{4}J = 3.64 Hz, 2H, 1 C$H_{\rm phen}$ + 1C$H_{\rm bpy}$), 7.64 (d, ^{3}J = 5.12 Hz, 1H, C$H_{\rm phen}$), 7.55 (dd, ^{3}J = 12.4 Hz, ^{3}J = 5.64 Hz, 2H, C$H_{\rm bpy}$), 7.47−7.40 (m, 3H, 2 C$H_{\rm bpy}$ + 1C$H_{\rm phen}$), 7.24 (m, 2H, C$H_{\rm bpy}$), 6.99 (d, ^{3}J = 8.6 Hz 1H, C$H_{\rm Ar}$), 6.90 (s, 1H, C$H_{\rm phen}$), 6.56 (t, 1H, NH), 4.66 (d, ^{3}J = 4.44 Hz, 2H, CH_2).

^{13}C NMR (CD$_3$CN, 100.6 MHz): δ 198.3; 161.6; 158.24; 158.23; 158.04; 158.00; 153.13; 152.97; 152.85; 152.78; 152.75; 149.3; 148.3; 144.4; 142.8; 138.72; 138.70; 138.59; 137.4; 134.9; 133.96; 133.74; 131.9; 130.8; 128.50; 128.46; 128.44; 128.34; 127.0; 125.9; 125.4; 125.22; 125.14; 125.13; 125.09; 121.7; 118.5; 100.7; 47.0.

^{19}F NMR (CD$_3$CN, 376.5 MHz): δ −151.6.

MS-ESI: *m*/*z* 371.5775, [M^{2+}] calcd. for C$_{40}$H$_{31}$N$_7$O$_2$Ru 371.5791.

C$_{40}$H$_{31}$B$_2$F$_8$N$_7$O$_2$Ru + H$_2$O: Anal. Calcd C 51.41, H 3.56, N 10.49; found C 50.84, H 3.53, N 10.10%.

[Ru(bpy)$_2$(H$_2$-L^2)](BF$_4$)$_2$. [Ru(bpy)$_2$(L^1)](BF$_4$)$_2$ (0.962 g, 1.05 mmol) and 4-phenylthiosemicarbazide (0.175 g, 1.05 mmol) were

refluxed for 16 h in a solvent mixture of ethanol and acetonitrile (2:1) under nitrogen. After evaporation to dryness the residue was solubilized in a minimum of acetonitrile, and the product was precipitated by addition of ethanol. The product was collected by filtration and dried under vacuum (0.83 g, 74%).

Decomposition point 245 °C.

^{1}H NMR (CD_3CN, 400 MHz): δ 8.70 (d, ^3J = 8.04 Hz, 1H, CH_{phen}), 8.26–8.18 (m, 4H, CH_{bpy}), 8.26 (s, 1H, CHN), 8.14 (d, ^3J = 7.56 Hz, 1H, CH_{Ar}), 8.10–8.03 (m, 3H, CH_{Ar}), 8.00–7.93 (m, 2H, CH_{Ar}), 7.81 (dd, ^3J = 16.08 Hz, ^3J = 4.84 Hz, 2H, CH_{Ar}), 7.68 (dd, ^3J = 8.2 Hz, ^3J = 5.04 Hz, 1H, CH_{Ar}), 7.62 (d, ^3J = 4.76 Hz, 1H, CH_{Ar}), 7.53 (dd, ^3J = 8.68 Hz, ^3J = 4.92 Hz, 2H, CH_{Ar}), 7.49–7.39 (m, 7H, CH_{Ar}), 7.33 (t, ^3J = 7.28 Hz, 2H, CH_{Ar}), 7.24–7.17 (m, 3H, CH_{Ar}), 6.93 (d, ^3J = 8.08 Hz, 1H, CH_{Ar}), 6.91 (s, 1H, CH_{Ar}), 6.50 (t, ^3J = 5.32 Hz, 1H, NH), 4.61 (m, 2H, CH_2).

^{13}C NMR (CD_3CN, 125.8 MHz): δ 158.2, 158.0, 153.0, 152.9, 152.8, 152.7, 149.3, 148.2, 144.6, 142.7, 138.7, 138.6, 134.8, 134.0, 131.9, 130.3, 129.4, 128.50, 128.45, 128.3, 126.9, 126.8, 126.2, 125.8, 125.4, 125.22, 125.14 125.09, 100.6, 47.4.

^{19}F NMR (CD_3CN, 376.5 MHz): δ −151.5

MS-ESI: 446.0982, [M^{2+}] calcd. for $C_{47}H_{38}N_{10}ORuS$ 446.0997.

$C_{47}H_{38}F_8N_{10}OB_2RuS$ + 2 H_2O: Anal. Calcd C 51.24, H 3.84, N 12.71; found C 50.92, H 3.33, N 12.45%.

[Ru(bpy)$_2$(L^2)MoO$_2$(MeOH)](BF$_4$)$_2$. [Ru(bpy)$_2$(H$_2$-L^2)](BF$_4$)$_2$ (100 mg, 0.094 mmol) and [MoO$_2$(acac)$_2$] (31 mg, 0.095 mmol) were refluxed for 18 h in a mixture of acetonitrile and methanol (1:1, 10 mL) and under an atmosphere of nitrogen. After filtration, the reaction mixture was evaporated to dryness. The residue was solubilized in acetonitrile and filtered. The solvent was evaporated, and the product was triturated with diethyl ether and washed with a small volume of dichloromethane, followed by diethyl ether, and dried under vacuum to yield a red crystalline solid (84 mg, 75%).

^{1}H NMR (CD_3CN, 500 MHz): δ 8.73 (s, 1H, CHN), 8.70 (d, ^3J = 8.6 Hz, 1H, CH_{phen}), 8.51–8.45 (m, 4H, CH_{bpy}), 8.16 (dd, ^3J = 8.4 Hz, ^4J = 1.1 Hz, 1H, CH_{phen}), 8.10–8.04 (m, 3H, 2 CH_{bpy} + 1CH_{phen}), 7.99–7.95 (m, 2H, CH_{bpy}), 7.88 (s, 1H, CH_{Ar}), 7.84–7.79 (m, 2H, CH_{bpy}), 7.71 (dd, ^3J = 8.55 Hz, ^3J = 5.25 Hz, 1H, CH_{phen}), 7.68–7.65 (m, 3H, CH_{Ar}), 7.63 (dd, ^3J = 5.15 Hz, ^4J = 1.2 Hz, 1H, CH_{phen}), 7.57–7.52 (m, 2H, CH_{bpy}), 7.45–7.39 (m, 3H, 2 CH_{bpy} + 1CH_{phen}), 7.33 (dd, ^3J = 8.45 Hz, ^3J = 7.5 Hz, 2H, CH_{Ar}), 7.24–7.21 (m, 2H, CH_{bpy}), 7.09 (t, ^3J = 7.4 Hz, 1H, CH_{Ar}), 6.98 (d, ^3J = 8.4 Hz, 1H, CH_{Ar}), 6.90 (s, 1H, CH_{phen}), 6.54 (t, ^3J = 5.9 Hz, 1H, NH), 4.67 (m, 2H, CH_2).

^{13}C NMR (CD_3CN, 125.8 MHz): δ 162.5, 159.7, 158.25, 158.23, 158.03, 158.00, 157.1, 153.1, 152.96, 152.84, 152.80, 152.7, 149.4, 148.2, 144.4, 142.8, 141.2, 138.72, 138.69, 138.58, 134.97, 134.85, 134.0, 133.7, 131.9, 129.8, 128.50, 128.45, 128.3, 127.0, 125.9, 125.4, 125.2, 125.14, 125.08, 124.4, 121.4, 121.2, 119.5, 100.7, 47.0.

^{19}F NMR (CD_3CN, 376.5 MHz): δ −151.7.

MS-ESI: m/z 510.0399, [M^{2+}-MeOH] calcd. for $C_{47}H_{36}MoN_{10}O_3RuS$ 510.0399.

$C_{48}H_{40}B_2F_8MoN_{10}O_4RuS$ + 2H_2O: Anal. Calcd C 45.77, H 3.52, N 11.12; found C 46.32, H 3.08, N 10.79%.

Determination of Quantum Yields. The emission quantum yields were determined at room temperature (RT) by using [Ru(bpy)$_3$]Cl$_2$ as reference and equation $\Phi_X = \Phi_{ref} \times$ (slope (X)/slope (ref)) $\times$ (η_X^2/η_{ref}^2), where Φ_X is the quantum yield of compound X, Φ_{ref} is the quantum yield of the reference compound ([Ru(bpy)$_3$]CL$_2$, Φ = 0.094 ± 0.004),[34] and η is the refraction index of the solvent. However, the term depending on the solvent was omitted, because acetonitrile was used as the solvent for all samples. The slope for each compound was obtained from the plot of integrated fluorescence intensity versus absorbance at five different concentrations (Figure 2b).

Time-Correlated Single-Photon Counting. The excited-state lifetimes were measured by time-correlated single-photon counting (TCSPC) in acetonitrile. Samples were deaerated and put under an argon atmosphere by freeze–pump–thaw technique in a cuvette with a degassing bulb. The light source was a pulsed laser at 470 nm (PEL-470) with a repetition rate set at 50 kHz for measurements up to 5 μs and 200 kHz for the shorter time range of 200 ns. The emission was detected with a photomultiplier tube with maximum sensitivity in the visible part of the spectrum. The excited-state decay was monitored at different emission wavelengths (580, 600, 620, 640, 660, and 680 nm). The slit width for detection was set to 10 nm, while the laser beam profile was ±10 nm.

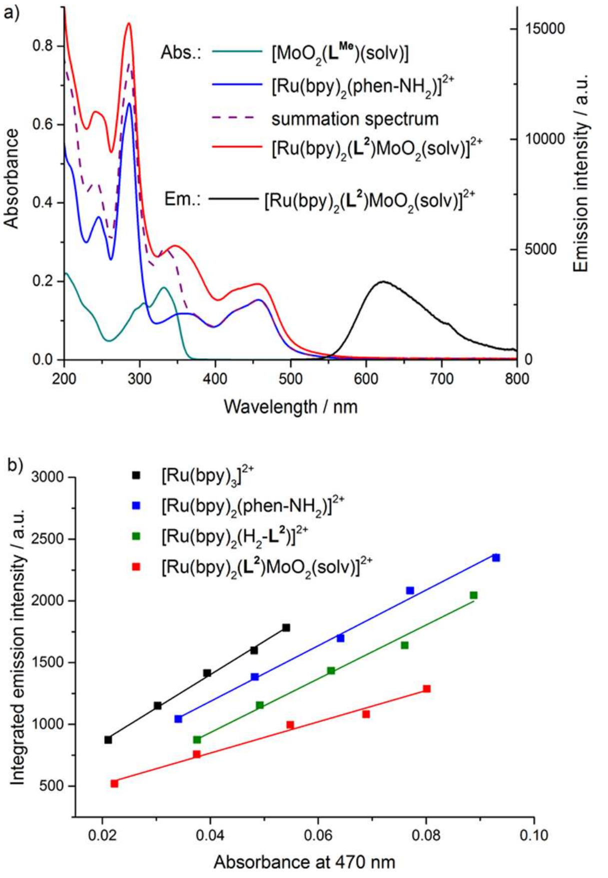

Figure 2. (a) Electronic absorption (red) and emission spectrum (black, λ_{exc} = 470 nm) of [Ru(bpy)$_2$(L^2)MoO$_2$(solv)]$^{2+}$ in comparison with the absorption spectra of [Ru(bpy)$_2$(phen-NH$_2$)]$^{2+}$ (blue) and [MoO$_2$(L^{Me})(solv)] (cyan) and the sum of their absorption spectra (purple), recorded at RT in deaerated MeCN, 10 μM concentration. (b) Plot of integrated emission intensity vs absorbance at 470 nm for solutions of [Ru(bpy)$_3$]$^{2+}$ (black), [Ru(bpy)$_2$(phen-NH$_2$)]$^{2+}$ (blue), [Ru(bpy)$_2$(H$_2$-L^2)]$^{2+}$ (green), and [Ru(bpy)$_2$(L^2)MoO$_2$(solv)]$^{2+}$ (red), where solv = coordinated solvent molecule, at a range of concentrations (1–6 μM, deaerated MeCN).

Electrochemistry. All electrochemical measurements were performed under nitrogen at RT. Cyclic voltammetry was performed with an EC epsilon potentiostat from BASi with a standard three-electrode electrochemical cell. Potentials were referenced to Ag/AgCl in NaCl$_{aq}$ (3 M). The working electrode was a carbon disk. The auxiliary electrode was a platinum wire. Tetrabutylammonium tetrafluoroborate (0.1 M) in dimethylformamide (DMF) was used as electrolyte.

Spectro-Electrochemistry. UV–vis spectro-electrochemical experiments were performed in the dark in a N$_2$-purged quartz cuvette of 1 mm path length equipped with a strip of carbon veil (Optiveil 12 g.m^2 area weight) as working electrode, a Pt wire, and a Ag/AgCl reference electrode. Tetrabutylammonium tetrafluoroborate 0.1 M in DMF was used as electrolyte. The potential was controlled by an EmStat potentiostat.

Photocatalytic Tests. Five samples (A–E) were tested in parallel. Solution A contained Ph$_3$P (300 mM), [Ru(bpy)$_2$(L^2)MoO$_2$(solv)](BF$_4$)$_2$ (1 mM), and methyl viologen dihexafluorophosphate (1 mM) in CD$_3$CN/deuterated dimethyl sulfoxide (DMSO-d_6;1:1 v/v, 0.7 mL). The solution was transferred into a gas-tight NMR tube and degassed via a minimum of three freeze−pump−thaw cycles using an acetone/liquid nitrogen bath for cooling and research-grade argon for equilibration. Four control samples were prepared in the same way. Sample B had the same composition as sample A but was kept in the dark. Sample C contained $[Ru(bpy)_2(\mathbf{H_2\text{-}L^2})]$ $(BF_4)_2$ (1 mM), 300 equiv of PPh_3, and 1 equiv of methyl viologen dihexafluorophosphate. Sample D contained $[Ru(bpy)_2(\mathbf{L^2})MoO_2(solv)](BF_4)_2$ (1 mM) and 300 equiv of PPh_3 but no methyl viologen dihexafluorophosphate. Sample E contained $[Ru(bpy)_3)]Cl_2$ (1 mM) plus $[MoO_2(\mathbf{L^{Me}})(solv)]$ (1 mM), 300 equiv of PPh_3, and 1 equiv of methyl viologen dihexafluorophosphate.

Samples A, C, D, and E were irradiated with a Philips 125 W medium-pressure mercury vapor lamp equipped with a water infrared filter and a cutoff filter ($\lambda > 435$ nm) for 17 h at a time followed by 7 h of storage in the dark, until almost complete conversion was reached by sample A (9 d). At the beginning and end of each irradiation period, the formation of $OPPh_3$ was monitored by ^1H and ^{31}P NMR spectroscopy (^1H NMR 500 MHz, ^{31}P 202.5 MHz) and by a photograph taken with and without flash to document changes in color and apparent emission intensity.

To account for the different lengths of time taken for the preparation of samples A−E, which required exposure to air and light, the turnover numbers were set to zero at the start of the first irradiation period. This allowed the direct comparison of the samples. In an additional control sample that contained Ph_3P (300 mM) in CD_3CN/DMSO-d_6 (1:1 v/v, 0.7 mL) under Ar and was left standing at RT for 9 d, only a trace amount of $OPPh_3$ could be detected by ^{31}P NMR.

Electron Paramagnetic Resonance Spectroscopy. The electron paramagnetic resonance (EPR) spectra were recorded at X band on a Jeol JES-REIX spectrometer. Samples were irradiated in situ with a 100 W mercury vapor arc equipped with a water infrared filter and a cutoff filter ($\lambda > 420$ nm). The general EPR parameters were: power 1 mW, field 336.2 mT, scan width ±7.5 mT, modulation width 0.1 mT, time constant 0.1 s, scan time 60 s, modulation frequency 100 kHz, and average of three scans at RT. Sample compositions and concentrations were as follows. Sample 1: $[Ru(bpy)_2(\mathbf{H_2\text{-}L^2})]^{2+}$ (0.25 mM) and MV^{2+} (0.25 mM) in acetonitrile; sample 2: $[Ru(bpy)_2(L^2)MoO_2(solv)]^{2+}$ (0.25 mM), PPh_3 (75 mM) and MV^{2+} (0.25 mM) in acetonitrile; and sample 3: $[Ru(bpy)_2(L^2)MoO_2(solv)]^{2+}$ (0.25 mM), PPh_3 (75 mM) and MV^{2+} (0.25 mM) in acetonitrile/DMSO (1:1 v/v). All measurements were performed in glass capillaries at RT and under Ar.

RESULTS AND DISCUSSION

Synthesis and Characterization of $[Ru(bpy)_2(L^2)MoO_2(MeOH)](BF_4)_2$, with H_2-L^2 = 2-Hydroxy-5-([1,10]-phenanthroline-5-ylaminomethyl)-benzaldehyde-*N*(1) phenylthiosemicarbazone. The photosensitizer $[Ru(bpy)_2(phen\text{-}NH_2)](BF_4)_2$ was prepared by adapting a procedure reported for the synthesis of the corresponding PF_6^- salt[33] and was used as a platform for the sequential synthesis of the catalytic unit (Scheme 2). 5-Chloromethyl-2-hydroxybenzaldehyde was prepared[32] and attached to the ruthenium complex via nucleophilic substitution. The resulting intermediate was condensed with commercially available 4-phenylthiosemicarbazide by adapting a published procedure.[35] The phenyl group was chosen to increase the hydrophobic character of the compound and to facilitate its isolation by precipitation. The photosensitizer-appended ligand $[Ru(bpy)_2(\mathbf{H_2\text{-}L^2})](BF_4)_2$ obtained was reacted with $[MoO_2(acac)_2]$ to produce dyad $[Ru(bpy)_2(\mathbf{L^2})MoO_2(MeOH)](BF_4)_2$. The product and intermediates were characterized by ^1H and ^{13}C NMR spectroscopy, ESI mass spectrometry, and elemental analyses (see Experimental Section).

Electronic Absorption and Emission Spectra. The electronic absorption spectrum of $[Ru(bpy)_2(\mathbf{L^2})MoO_2(MeOH)](BF_4)_2$, dissolved in MeCN, shows an intense band in the range of 235−250 nm (ε_{242} = 71 900 M^{-1} cm^{-1}), ligand-centered (LC) transitions at 285 nm (ε_{285} = 98 000 M^{-1} cm^{-1}) and 345 nm (ε_{345} = 32 900 $M^{-1}cm^{-1}$), and a Ru-based metal-to-ligand (MLCT) transition at 455 nm (ε_{455} = 21 700 M^{-1} cm^{-1}). Figure 2a shows the absorption spectrum of $[Ru(bpy)_2(\mathbf{L^2})MoO_2(solv)]^{2+}$ in comparison with the absorption spectra of the two individual components of the dyad, namely, $[Ru(bpy)_2(phen\text{-}NH_2)]^{2+}$ and $[MoO_2(\mathbf{L^{Me}})$ (solv)], with $\mathbf{H_2\text{-}L^{Me}}$ = *para*-methylbenzaldehyde-*N*(1)-ethylsemicarbazone[28] and solv = MeOH or MeCN, (Scheme 2), and the sum of their spectra. It is evident that the absorbance above 375 nm is dominated by transitions associated with the Ru-based component of the dyad. Excitation into the low-energy MLCT band at 470 nm gives rise to a broad emission band with a maximum at 620 nm (Figure 2a). As expected, the attachment of the Mo-based catalytic unit leads to a slight change in the position and intensity of the absorption and emission bands compared with those reported for the parent photosensitizer $[Ru(bpy)_2(phen)]^{2+}$ ($\lambda_{max,abs}$ = 449 nm, ε_{449} = 15 700 M^{-1} cm^{-1}, $\lambda_{max,em}$ = 618 nm, MeCN).[36,37]

If solutions with equal absorbance at 470 nm are compared, the emission intensity of the molybdenum-containing dyad $[Ru(bpy)_2(\mathbf{L^2})MoO_2(solv)]^{2+}$ is lower than that of the thiosemicarbazone-appended photosensitizer $[Ru(bpy)_2(\mathbf{H_2\text{-}L^2})]^{2+}$ (Figure 2b). The linear relationship between the integrated luminescence intensity and the absorbance of solutions of both $[Ru(bpy)_2(\mathbf{H_2\text{-}L^2})]^{2+}$ and $[Ru(bpy)_2(\mathbf{L^2})MoO_2(solv)]^{2+}$ at a range of different concentrations confirms the absence of intermolecular quenching (Figure 2b).

Time-Correlated Single-Photon Counting. The luminescence decay kinetics of $[Ru(bpy)_2(\mathbf{L^2})MoO_2(solv)]^{2+}$, $[Ru(bpy)_2(phen\text{-}NH_2)]^{2+}$, and $[Ru(bpy)_2(\mathbf{H_2\text{-}L^2})]^{2+}$ were investigated by TCSPC. In an additional control experiment, $[Ru(bpy)_2(\mathbf{L^2})MoO_2(solv)]^{2+}$ was investigated in the presence of Ph_3P (100-fold excess) to assess whether or not Ph_3P quenches the emission of the dyad. The samples were dissolved in MeCN and excited at 470 nm, and time-resolved emission data were collected at the maximum of the emission band at 620 nm (Figure 3 and Table 1). The emission decay curve obtained for $[Ru(bpy)_2(phen\text{-}NH_2)]^{2+}$ could be fitted using a single exponential. The lifetime τ of 1100 ± 1 ns obtained is slightly longer than that reported for the parent photosensitizer $[Ru(bpy)_2(phen)]^{2+}$, which was obtained under similar conditions and also fitted to a single exponential (τ = 830 ns, λ_{exc} = 450 nm, λ_{em} = 600 nm, MeCN, RT).[37,37]

The emission decay of $[Ru(bpy)_2(\mathbf{H_2\text{-}L^2})]^{2+}$ required a double exponential fit, indicating that there are two ^{3}MLCT excited states contributing to the emission. The lifetime of the major, longer-lived component of 1100 ± 2 ns (60%) is identical with the lifetime of $[Ru(bpy)_2(phen\text{-}NH_2)]^{2+}$, while the shorter-lived, minor component has a lifetime of 303 ± 1 ns (40%). Hence, the two excited states may tentatively be assigned to bpy- and $\mathbf{H_2\text{-}L^2}$-localized ^{3}MLCT states, respectively, taking into account that the distribution deviates slightly from the statistical distribution of 66% and 33%. Dual emission is frequently observed in heteroleptic Ru(II) complexes of this type.[37,38]

The emission decay of the dyad $[Ru(bpy)_2(\mathbf{L^2})MoO_2(solv)]^{2+}$ required a three-component fit. The lifetime

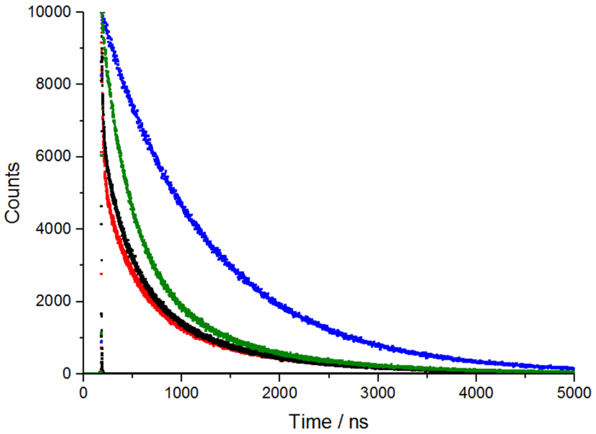

Figure 3. Emission decay profiles obtained at 620 nm (λ_{exc} = 470 nm) under Ar for 1 × 10^{-5} M solutions of $[Ru(bpy)_2(phen\text{-}NH_2)]^{2+}$ (blue), $[Ru(bpy)_2(\mathbf{H_2\text{-}L^2})]^{2+}$ (green), $[Ru(bpy)_2(\mathbf{L^2})MoO_2(solv)]^{2+}$ (red), and $[Ru(bpy)_2(\mathbf{L^2})MoO_2(solv)]^{2+}$ with 100-fold excess of Ph_3P (black) in MeCN.

Table 1. Quantum Yields (Φ) of Luminescence and Lifetimes (τ) of the ^{3}MLCT States in MeCN

	Φ_{470}[a]	τ (ns)[b]
$[Ru(bpy)_2(phen\text{-}NH_2)]^{2+}$	0.078 ± 0.003	1100 ± 1
$[Ru(bpy)_2(\mathbf{H_2\text{-}L^2})]^{2+}$	0.076 ± 0.003	303 ± 1 (40%), 1100 ± 2 (60%)
$[Ru(bpy)_2(\mathbf{L^2})MoO_2(solv)]^{2+}$	0.044 ± 0.002	11.9 ± 0.1 (2%), 320 ± 1 (31%), 1149 ± 2 (67%)
$[Ru(bpy)_2(\mathbf{L^2})MoO_2(solv)]^{2+}$ + Ph_3P	not determined	8.1 ± 0.1 (1%), 290 ± 1 (31%), 1037 ± 1 (68%)

[a] Argon atmosphere, 1 × 10^{-5} M in MeCN, $[Ru(bpy)_3]Cl_2$ reference: Φ = 0.094 ± 0.004,[34] λ_{exc} = 470 nm, λ_{em} = 620 nm, error margins represent one standard deviation and are propagated from the standard error in the fitted gradients (plot shown in Figure 2b). [b] λ_{exc} = 470 nm, λ_{em} = 620 nm. Error margins represent one standard deviation.

of the longest-lived component of 1149 ± 2 ns resembles those obtained for $[Ru(bpy)_2(phen\text{-}NH_2)]^{2+}$ and $[Ru(bpy)_2(\mathbf{H_2\text{-}L^2})]^{2+}$, and the close to statistical contribution of 67% suggests that it is due to decay from a bpy-localized excited state. The second lifetime of 320 ± 1 ns resembles that of the shorter-lived component obtained for $[Ru(bpy)_2(\mathbf{H_2\text{-}L^2})]^{2+}$, and again, the close to statistical contribution of 31% indicates decay from a $\mathbf{H_2\text{-}L^2}$-centered excited state. An additional minor (2%) short-lived component with τ = 11.9 ± 0.1 ns had to be added to fit the data satisfactorily.

The spectroscopic investigations show that the covalently linked catalytic unit of the dyad decreases the quantum yield of the photoactive unit. On the one hand, in similar systems, quenching via intramolecular photoinduced electron transfer from an appended electron-rich phenolate ligand to a photoexcited metal-based luminophore, such as $Ru^{III}\text{-}bpy^{\bullet-}$, has been observed using time-resolved absorption spectroscopy.[39] On the other hand, the addition of a 100-fold excess of PPh_3 does not have a significant effect on the three lifetimes obtained for $[Ru(bpy)_2(\mathbf{L^2})MoO_2(solv)]^{2+}$ (Figure 3 and Table 1), confirming the absence of an intermolecular quenching effect of the substrate.

Electrochemistry. The cyclic voltammogram (CV) of $[Ru(bpy)_2(\mathbf{L^2})MoO_2(solv)](BF_4)_2$, recorded between −2 and 1.7 V in dry DMF using $[Bu_4N](BF_4)$ as the supporting electrolyte, shows several redox processes that are also evident in the CVs of its components (Figure 4, Figures S1−S3, and Table 2). In the positive region, an irreversible oxidation wave is observed that involves the transfer of approximately two electrons, based on the comparison with the peak currents associated with the reversible processes in the negative potential region. One of the overlapping oxidation steps can be assigned to the oxidation of Ru(II) to Ru(III) by comparison with electrochemical data obtained for $[Ru(bpy)_3]Cl_2$ under analogous conditions (Table 2 and Figure S1), previously reported oxidation potentials for similar Ru(II) complexes,[33] and spectro-electrochemical investigations (see below). The overlapping second irreversible oxidation process is associated with the molybdenum-coordinated thiosemicarbazone. A comparison with the CVs obtained for $[MoO_2(\mathbf{L^{Me}})(solv)]$ and $\mathbf{H_2\text{-}L^{Me}}$ under analogous conditions (Figures S2 and S3), and observations reported for similar Mo(VI)-semicarbazone complexes,[40,41] provide further evidence for this assertion. It is known that a one-electron oxidation of thiosemicarbazones can lead to dimerization via disulfide-bond formation, while a two-electron oxidation can lead to cyclization and formation of 1,2,4-triazole-3-thione or 1,3,4-thiadiazole rings.[42] The latter is in accordance with the irreversibility and high peak current of the oxidation process observed at a peak potential ($E_{p,ox}$) of 1.43 V in the CV of $[MoO_2(\mathbf{L^{Me}})(solv)]$ (Table 2).

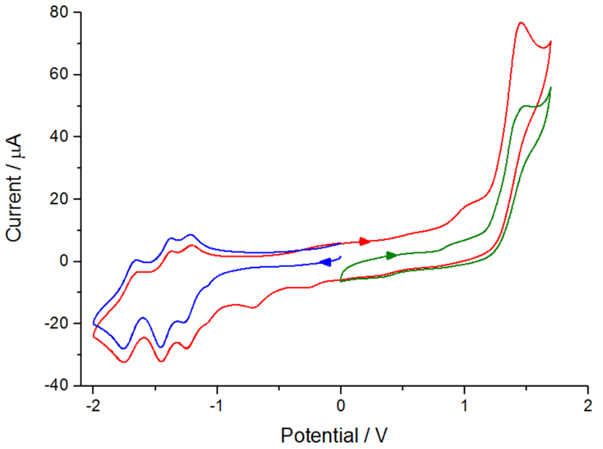

Figure 4. CV of $[Ru(bpy)_2(\mathbf{L^2})MoO_2(solv)](BF_4)_2$ (scan range: from 0 to +1.7 V and from −2.0 to 0 V (red); between 0 and +1.7 V (green) and between 0 and −2 V (blue); 1 mM with 0.1 M $[Bu_4N](BF_4)$ in anhydrous DMF, potentials vs Ag/AgCl, scan rate 100 mV s^{-1}.

In addition, there are weak irreversible waves at $E_{p,ox}$ = 0.58 and 1.07 V and $E_{p,red}$ = −0.27, −0.72, and −1.12 V that can be assigned to the Mo-containing unit and/or its degradation products as similar waves are observed in the CV of $[MoO_2(\mathbf{L^{Me}})(solv)]$ (Figure S2). While the shoulder at −1.12 V lies within the potential range typically associated with the reduction of Mo(VI) to Mo(V),[40,41] the irreversible reduction waves at −0.27 and −0.72 V are only present if the positive potential range is scanned first (Figure 4). Hence, these two reduction processes appear to be associated with chemical reaction products formed upon oxidation.

By comparison with the CV of $[Ru(bpy)_3]Cl_2$ (Table 2 and Figure S1) and literature data,[33] the three reversible waves at $E_{1/2}$ = −1.22, −1.41, and −1.75 V can be assigned to three successive one-electron reductions of the Ru-polypyridine unit.

DOI: 10.1021/acs.inorgchem.6b01485
Inorg. Chem. XXXX, XXX, XXX−XXX

Table 2. Electrochemical Data

complex	$E_{1/2}$/V (ΔE_p/mV) $[Ru(polypy)_3]^{0/-}$	$E_{1/2}$/V (ΔE_p/mV) $[Ru(polypy)_3]^{+/0}$	$E_{1/2}$/V (ΔE_p/mV) $[Ru(polypy)_3]^{2+/+}$	$E_{p,ox}$/V (Ru^{II}/Ru^{III})
$[Ru(bpy)_2(\mathbf{L}^2)\text{-}MoO_2(solv)](BF_4)_2$	−1.75 (120)	−1.41 (80)	−1.22 (60)	1.46
$[Ru(bpy)_3]Cl_2$	−1.68 (90)	−1.37 (70)	−1.19 (60)	1.41
compound		$E_{p,red}$/V (Mo unit)	$E_{p,ox}$/V (Mo unit)	
$[Ru(bpy)_2(\mathbf{L}^2)\text{-}MoO_2(solv)](BF_4)_2$		−1.12, −0.72, −0.27	∼1.0, 1.46	
$[MoO_2(\mathbf{L}^{Me})(solv)]$		−1.14, ∼0.7, ∼0.3	1.07, 1.43	
compound		$E_{1/2}$/V (ΔE_p/mV) $MV^{0/+}$	$E_{1/2}$/V (ΔE_p/mV) $MV^{+/2+}$	
methyl viologen (MV) dichloride		−0.73 (80)	−0.35 (80)	

[1] 1 mM solutions in degassed anhydrous DMF with 0.1 M $[Bu_4N](BF_4)$ as supporting electrolyte, potentials vs Ag/AgCl, scan rate 100 mV s^{-1}.

Spectro-Electrochemical Oxidation. $[Ru(bpy)_2(\mathbf{L}^2)\text{-}MoO_2(solv)](BF_4)_2$ was oxidized electrochemically at 1.5 V using a carbon veil electrode, and the difference absorption spectra were recorded (Figure 5). Two negative bands (bleaches) developed over time at 360 and 470 nm, while the absorbance below 340 nm increased, and a weak and broad band developed above 500 nm. Bleaching in the visible region of the broad MLCT band of the dyad is consistent with the oxidation of Ru(II) to Ru(III). However, the relative intensity of the two apparent bleaches at 360 and 470 nm differs from that observed by Lomoth et al. for $[Ru(bpy)_3]^{2+}$ in acetonitrile[43] and indicates the presence of another chromophore. Likewise, the fact that the isosbestic point at 332 nm gradually disappears after ∼15 min of electrolysis is consistent with the formation of another oxidized species.

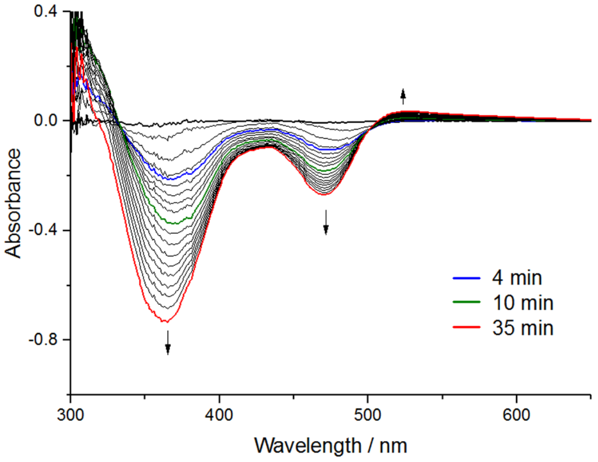

Figure 5. Difference spectra obtained during the spectro-electrochemical oxidation of $[Ru(bpy)_2(\mathbf{L}^2)MoO_2(solv)](BF_4)_2$ (0.5 mM), recorded at E_{app} = 1.5 V after 5 s and after 1, 2, 3, 4, 5, 6, 7, 8, 10, 12, 14, 16, 18, 20, 23, 26, 30, and 35 min (carbon veil electrode).

For comparison, the reference compound $[MoO_2(\mathbf{L}^{Me})(MeOH)]$, which can be considered as representative of the catalytic moiety of the dyad, was oxidized under conditions analogous to those used for the oxidation of the dyad (Figure 6). In $[MoO_2(\mathbf{L}^{Me})(MeOH)]$, the molybdenum is already in its group oxidation state +VI and cannot oxidize further, yet significant spectroscopic changes are observed in the visible region of the spectra. Overall, the absorbance at 295 and 350 nm increases, while the absorbance at 320 nm and between 370 and 500 nm decreases.

Interestingly, after 10 min of electrolysis, four isosbestic points emerge at 282, 310, 332, and 370 nm and point toward the clean interconversion of two defined chromophores. Hence, the initial oxidation of the phenol−thiosemicarbazone ligand triggers subsequent chemical change(s), consistent with the irreversible redox wave seen in the CV of $[MoO_2(\mathbf{L}^{Me})(MeOH)]$ (Figure S2). It is conceivable that the initial ligand oxidation causes a change in the coordination environment, which may be followed by an oxidative dimerization or, more likely, an intramolecular cyclization of the ligand, as reported for structurally related thiosemicarbazones.[42]

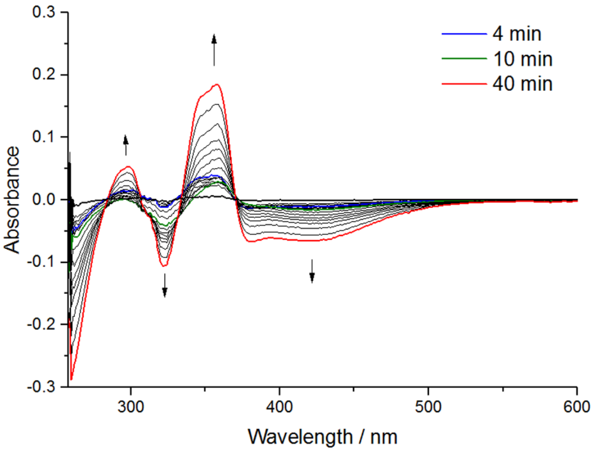

Figure 6. Difference spectra obtained during the spectro-electrochemical oxidation of $[MoO_2(\mathbf{L}^{Me})MeOH]$ (0.5 mM) recorded at E_{app} = 1.5 V after 1, 2, 3, 4, 6, 8, 10, 12, 15, 18, 21, 25, 30, 35, and 40 min (carbon veil electrode).

While the bleach observed at 323 nm is consistent with the gradual disappearance of the isosbestic point at 323 nm and the bleach in the dyad spectra, the absorbance increase at ∼359 nm is not reflected in the spectra of dyad. Hence, not all of the spectro-electrochemical features of the dyad can be attributed to contributions from its two components.

Spectro-Electrochemical Reduction. The spectroscopic profiles obtained upon electrochemical reduction (−1.2 V) are shown in Figure 7. Two positive bands rise at 390 and 510 nm as well as two negative bands at 350 and 450 nm.

Similarly, $[Ru(bpy)_3]Cl_2$ and $[MoO_2(\mathbf{L}^{Me})(MeOH)]$ were reduced at the same potential (Figures S5 and S6). A comparison of the spectra obtained for the complexes shows that the dyad behaves similarly to $[Ru(bpy)_3]Cl_2$ above 400 nm, while the spectral changes observed below 400 nm are consistent with the reduction of both the ruthenium and the molybdenum moieties.

A reduction of the dyad was then performed at −1 V (Figure 8a) to investigate if it is possible to selectively reduce only the Mo-based catalytic center. The profile obtained is very different

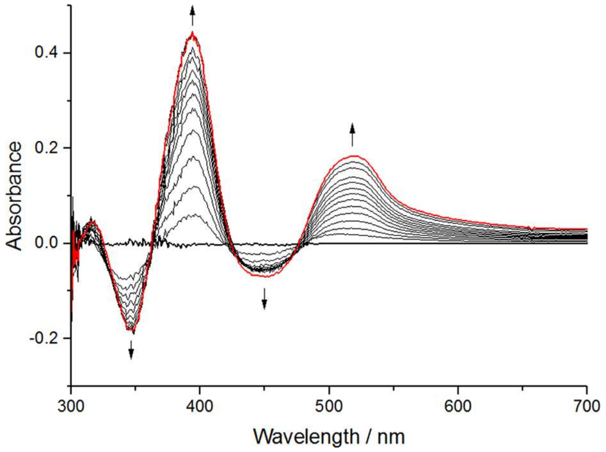

Figure 7. Difference absorption spectra obtained during the spectroelectrochemical reduction of $[Ru(bpy)_2(\mathbf{L}^2)MoO_2(solv)](BF_4)_2$ (0.5 mM), recorded at $E_{app} = -1.2$ V after 0, 1, 2, 3, 4, 5, 6, 7, 8, 9, 10, 12, 14, and 18 min (carbon veil electrode).

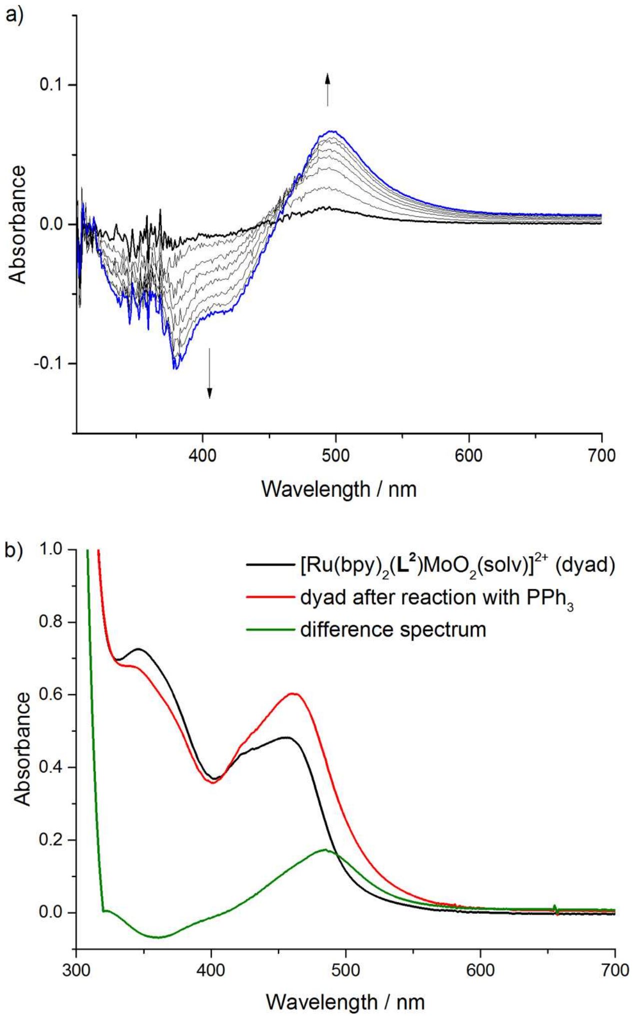

Figure 8. (a) Difference spectra obtained during the spectroelectrochemical reduction of $[Ru(bpy)_2(\mathbf{L}^2)MoO_2(solv)](BF_4)_2$ (0.5 mM), recorded at $E_{app.} = -1$ V after 10, 30, 60, and 90 s and 2, 3, 4, and 6 min (carbon veil electrode); (b) electronic absorption spectrum of $[Ru(bpy)_2(\mathbf{L}^2)MoO_2(solv)](BF_4)_2$ (25 μM) in MeCN before (black) and after reaction with Ph_3P (2.5 mM) (red) and the corresponding difference spectrum (green).

from that recorded for the dyad upon reduction at the more negative potential of −1.2 V (Figure 7). A positive band at 490 nm and three overlapping negative bands in the region between 300 and 450 nm grow in over time. The positive band resembles the corresponding band in the spectrum of the molybdenum complex (Figure 8b). Despite the absence of the small positive band at 360 nm, the absorbance between 300 and 450 nm decreases, whereas it increases when $[Ru(bpy)_3]Cl_2$ is reduced.

The spectrum obtained upon electrochemical reduction of $[Ru(bpy)_2(\mathbf{L}^2)MoO_2(solv)](BF_4)_2$ at −1 V was then compared with the spectrum obtained after the stoichiometric chemical reduction of the dyad, which was performed at a 25 μM concentration in MeCN in the absence of an O atom donor. To ensure complete reduction of the Mo-based unit (turnover number = 0.5) a 100-fold excess of the O atom acceptor PPh_3 was used. The initial spectrum of $[Ru(bpy)_2(\mathbf{L}^2)MoO_2(solv)](BF_4)_2$ was subtracted from the spectrum recorded after chemical reduction, to obtain a difference spectrum (Figure 8b). The profiles of the spectra obtained after electrochemical and chemical reduction are very similar. Therefore, the spectroelectrochemical measurements confirm that the molybdenum-based moiety can be selectively reduced at −1 V, while the reduction of the ruthenium-based moiety requires a more negative potential.

Photoactivated Oxygen Atom Transfer Catalysis. The catalytic activity of the dyad was investigated using triphenyl phosphine as the oxygen acceptor and DMSO as the oxygen donor. Under an atmosphere of argon, a solution containing $[Ru(bpy)_2(\mathbf{L}^2)MoO_2(solv)]^{2+}$ (1 mM), triphenyl phosphine (300 equiv), and methyl viologen (MV^{2+}, 1 equiv) in a mixture of deuterated acetonitrile/DMSO (1:1 v/v; sample A) was subjected to alternating cycles of irradiation with >435 nm light (17 h) followed by dark storage (7 h). At the beginning and end of each irradiation period, the formation of triphenyl phosphine oxide was monitored by ^1H and ^{31}P NMR spectroscopy. As evident from Figure 9, the reaction proceeded significantly faster during the periods of light exposure than in the dark. After a total irradiation time of 154 h, 95% completion was reached, and the presence of dimethyl sulfide in the sample was clearly detectable by its characteristic smell. The catalyst proved to be remarkably stable under these conditions, with the turnover number only limited by the solubility of triphenyl phosphine in DMSO/acetonitrile (1:1 v/v). The ^1H NMR spectra of sample A were examined before and after each irradiation period to monitor the integrity of the catalyst. Even after a total irradiation time of 154 h, the proton resonances of the dyad remained essentially unchanged (Figure S8).

A control experiment in which an analogous solution was kept in the dark all the time (sample B, Figure 9) produced much less of the oxidation product, indicating that the thermal conversion rate is much slower than the photochemical conversion. Again, the ^1H NMR spectra recorded during the thermal reaction showed no evidence for either catalyst decomposition or the formation of LMo(O)-O-Mo(O)L dimers (Figure S9). A control sample containing $[Ru(bpy)_2(\mathbf{L}^2)MoO_2(solv)]^{2+}$ (1 mM) and 300 equiv of triphenylphosphine but no methyl viologen (sample D) yielded a similar amount of product to the dark control after irradiation for a total of 154 h (Figure 9), demonstrating that methyl viologen accelerates the reaction in the presence of light. A control sample containing $[Ru(bpy)_2(\mathbf{H_2\text{-}L}^2)]^{2+}$ but no molybdenum (sample C) was found to produce less

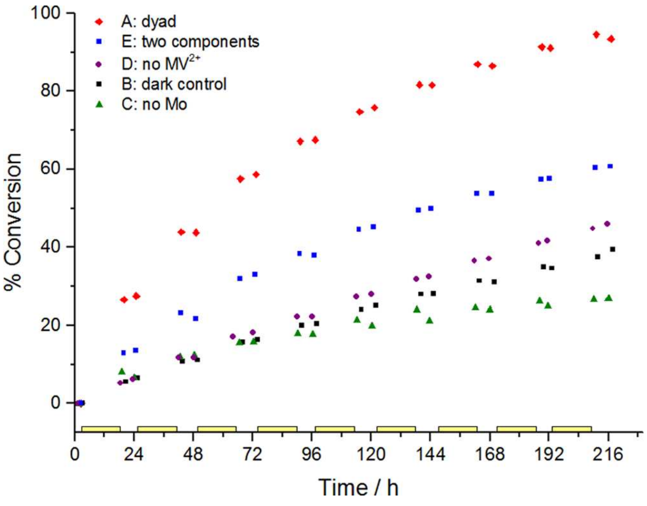

Figure 9. Performance of selected catalysts and control systems in the oxidation of PPh_3 during alternating cycles of irradiation with >435 nm light (17 h, indicated by yellow bars) followed by storage in the dark (7 h). Conditions used: deuterated acetonitrile/DMSO (1:1 v/v), Ar atmosphere, RT, (sample A: $[Ru(bpy)_2(\mathbf{L^2})MoO_2(solv)]^{2+}$, 300 equiv of PPh_3 and 1 equiv of MV^{2+}; sample B: control kept in the dark; sample C: $[Ru(bpy)_2(\mathbf{H_2\text{-}L^2})]^{2+}$, 300 equiv of PPh_3 and 1 equiv of MV^{2+}; sample D: $[Ru(bpy)_2(\mathbf{L^2})MoO_2(solv)]^{2+}$, 300 equiv of PPh_3 but no MV^{2+}; sample E: $[Ru(bpy)_3)]^{2+}$ plus $[MoO_2(\mathbf{L^{Me}})$ (solv)], 300 equiv of PPh_3, and 1 equiv of MV^{2+}).

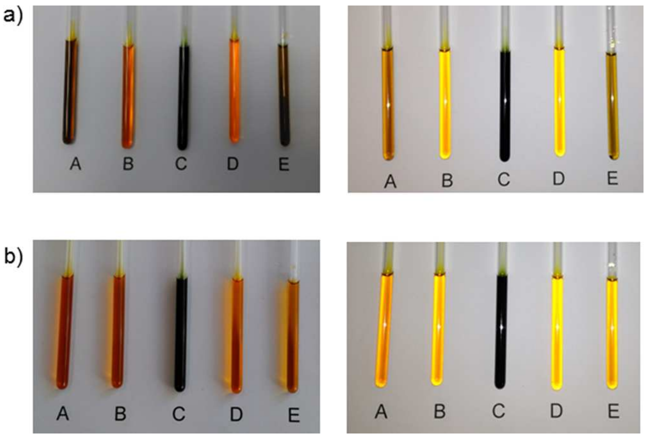

Figure 10. Photographs of samples A–E taken immediately after irradiation (a) and after storage in the dark (b), both without (left) and with (right) flash (sample A: $[Ru(bpy)_2(\mathbf{L^2})MoO_2(solv)]^{2+}$, 300 equiv of PPh_3 and 1 equiv of MV^{2+}; sample B: control kept in the dark; sample C: $[Ru(bpy)_2(\mathbf{H_2\text{-}L^2})]^{2+}$, 300 equiv of PPh_3 and 1 equiv of MV^{2+}; sample D: $[Ru(bpy)_2(\mathbf{L^2})MoO_2(solv)]^{2+}$, 300 equiv of PPh_3 but no MV^{2+}; sample E: $[Ru(bpy)_3]^{2+}$ plus $[MoO_2(\mathbf{L^{Me}})(solv)]$, 300 equiv of PPh_3 and 1 equiv of MV^{2+}).

triphenylphosphine oxide after irradiation for the same period of time than the dark control. The last experiment confirms that the molybdenum(VI) dioxo unit increases the reaction rate by catalyzing the OAT between dimethyl sulfoxide and triphenylphosphine.

When $[Ru(bpy)_3]^{2+}$ and $[MoO_2(\mathbf{L^{Me}})(solv)]$ were tested in a solution that contained the two individual components separately in a 1:1 ratio (sample E), a significant amount of triphenyl phosphine oxide was produced but ~35% less than with the dyad. The comparison of the catalytic activity of the dyad with the two-component system indicates that the intramolecular electron transfer between the photosensitizer and the catalytic center is more efficient than intermolecular electron transfer between two individual components.

Mechanistic information can be gathered from a comparison of the color and luminescence of the samples before and after each irradiation cycle. Therefore, after each irradiation and dark period, photographs of samples A, C, D, and E were taken both with and without flash to document any changes in emission intensity and color, respectively, in comparison with sample B, which was kept in the dark (Figure 10).

Initially, all five solutions were bright orange (Figure S7). Upon irradiation, the sample containing $[Ru(bpy)_2(\mathbf{H_2\text{-}L^2})]^{2+}$ (sample C) changed color from orange to dark green, and the emission was lost due to the oxidative quenching of the Ru(II)* excited state by MV^{2+} leading to the formation of $MV^{\bullet+}$, which strongly absorbs at the emission wavelength. (Figure 10a).[43] In the absence of the *cis*-dioxo molybdenum center, the dark green color remained, even after storage of the sample for 7 h in the dark. In this sample, a subsequent OAT could not take place, since the catalytic Mo center was missing.

Upon irradiation, samples A and E, $[Ru(bpy)_2(\mathbf{L^2})\text{-}MoO_2(solv)]^{2+}$ and $[Ru(bpy)_3]^{2+}$ plus $[MoO_2(\mathbf{L^{Me}})$ (solv)], respectively, changed color from bright orange to brown, and the intensity of the apparent emission decreased (Figure 10a). These observations are consistent with a mixture that contains the orange and luminescent Ru(II)-based photosensitizer unit and dark blue-green $MV^{\bullet+}$, one of the products of the oxidative quenching of the Ru^{III}-bpy/phen$^{\bullet-}$ ^{3}MLCT excited state by MV^{2+}, which initially produces Ru^{III}-bpy/phen and $MV^{\bullet+}$. While in the absence of other reductants, back electron transfer from $MV^{\bullet+}$ to Ru^{III} occurs on the nanosecond time scale,[43] in our case the $MV^{\bullet+}$ radical is much longer-lived (see below). In accordance with the irreversible oxidation wave seen in the CV of the dyad and its emission lifetimes, we propose that fast reduction of the Ru^{III} center occurs via electron transfer from the thiosemicarbazone ligand of the Mo complex rather than back electron transfer from $MV^{\bullet+}$. To confirm this proposal, the absorption spectra of sample A were recorded before irradiation, immediately after selected irradiation intervals, and after storage in the dark. The characteristic absorption bands due to $MV^{\bullet+}$ at λ_{max} 397 and 609 nm emerge during irradiation (Figure 11).[43] Bleaching of the ^{3}MLCT band (λ_{max} = 455 nm), which would be expected upon oxidation of Ru^{II} to Ru^{III}, is not observed. Consequently, the rereduction of the photooxidized Ru^{III} to Ru^{II} has occurred on the time scale that it took to record the absorption spectrum (~2 min). However, the $MV^{\bullet+}$ radical is still present and hence is not the source of the reducing equivalent.

During the storage periods in the dark, the color of both NMR samples (A and E) returned to orange, and the emission was restored, indicating that the resting state of the Ru(II)-based photosensitizer is regenerated and the $MV^{\bullet+}$ radical cation is reoxidized to MV^{2+} (Figure 10b). Light is not required for this reaction to proceed. The electronic absorption spectra confirm a decrease in the MV^{+} concentration in the dark, with the spectrum resembling that obtained after 1 h of irradiation (Figure 11).

Electron Paramagnetic Resonance Spectroscopy. In addition, EPR spectroscopy was used to monitor radical formation. During in situ irradiation of a solution containing $[Ru(bpy)_2(\mathbf{H_2\text{-}L^2})]^{2+}$ (0.25 mM) and MV^{2+} (0.25 mM) in acetonitrile, a strong EPR signal due to MV^{+} was observed (Figure 12, Sample 1).[44] Even 1 h after stopping the irradiation,

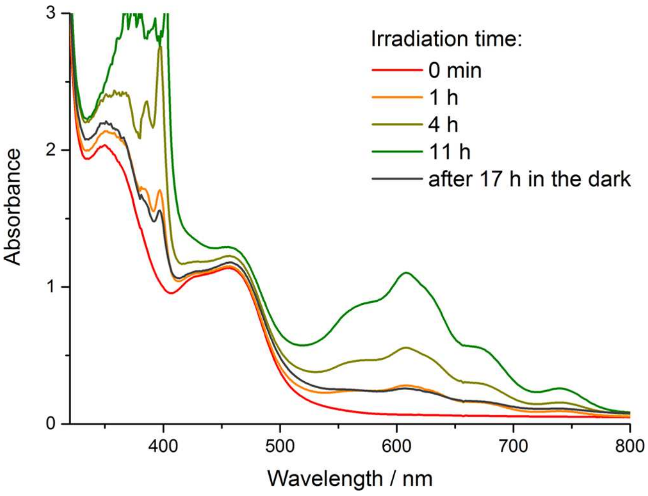

Figure 11. Electronic absorption spectra of a dilute solution of sample A recorded before irradiation, immediately after selected irradiation intervals, and after subsequent storage in the dark. Conditions: $[Ru(bpy)_2(L^2)MoO_2(solv)]^{2+}$ (0.25 mM), PPh_3 (75 mM), and MV^{2+} (0.25 mM) in acetonitrile/DMSO 1:1 v/v, RT, Ar, 0.2 cm path length.

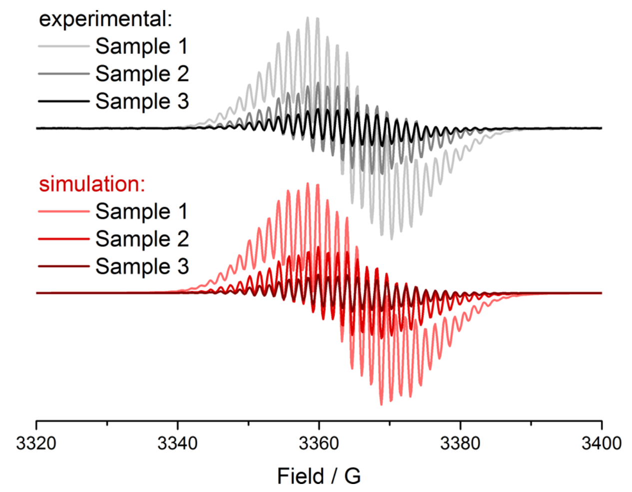

Figure 12. EPR spectra obtained during in situ irradiation of Sample 1: $[Ru(bpy)_2(\mathbf{H_2\text{-}L^2})]^{2+}$ (0.25 mM) and MV^{2+} (0.25 mM) in acetonitrile, Sample 2: $[Ru(bpy)_2(\mathbf{L^2})MoO_2(solv)]^{2+}$ (0.25 mM), PPh_3 (75 mM) and MV^{2+} (0.25 mM) in acetonitrile, and Sample 3: $[Ru(bpy)_2(\mathbf{L^2})MoO_2(solv)]^{2+}$ (0.25 mM), PPh_3 (75 mM) and MV^{2+} (0.25 mM) in acetonitrile/DMSO (RT, Ar); simulated spectra are shown in red; simulation parameters are listed in Table S1.

66% of the original $MV^{\bullet+}$ signal remained, confirming that the radical is long-lived and back electron transfer from $MV^{\bullet+}$ to the complex, most likely an oxidized form of the ligand $\mathbf{H_2\text{-}L^2}$, is very slow. However, a $\mathbf{H_2\text{-}L^2}$-based radical could not be detected, since the spectrum was dominated by the intense $MV^{\bullet+}$ signal.

During in situ irradiation of a sample containing $[Ru(bpy)_2(\mathbf{L^2})MoO_2(solv)]^{2+}$ (0.25 mM), PPh_3 (75 mM), and MV^{2+} (0.25 mM) in acetonitrile (no DMSO), a clear signal due to $MV^{\bullet+}$ was observed (Figure 12, Sample 2). In line with the lower quantum yield of the dyad, the signal was weaker than that observed with $[Ru(bpy)_2(\mathbf{H_2\text{-}L^2})]^{2+}$. An $\mathbf{L^2}$-based radical or paramagnetic Mo species could not be detected. Again, the strong signal of the exceptionally stable $MV^{\bullet+}$ radical is likely to mask any signals of shorter-lived radical species.

Subsequently, DMSO was added to the dyad-containing sample, and the EPR spectrum was recorded, while the sample was irradiated. In this case, a weaker signal due to $MV^{\bullet+}$ was observed (Figure 12, Sample 3). The decrease is consistent with the expected decrease of the $MV^{\bullet+}$ concentration under turnover conditions. In the dark, the signal decayed, with ~33% of the original intensity remaining after 1 h. Again, ligand- or Mo-based signals could not be detected, since the spectrum was dominated by the $MV^{\bullet+}$ signal.

Proposed Catalytic Cycle. On the basis of our observations and the information obtained from photophysical, spectroscopic, and electrochemical investigations, the following catalytic mechanism is proposed (Scheme 3). In the first step of the photoredox cycle, the photoexcited dyad $[Ru^{II}{*}(bpy)_2(\mathbf{L^2})Mo^{VI}O_2(solv)]^{2+}$ is oxidatively quenched by MV^{2+} to give $[Ru^{III}(bpy)_2(\mathbf{L^2})Mo^{VI}O_2(solv)]^{2+}$ and $MV^{\bullet+}$, as evidenced by the change in color from orange to dark blue-green, the EPR spectra, and the loss of emission. The oxidized dyad then undergoes fast intramolecular electron transfer to form $[Ru^{II}(bpy)_2(L^2)^+Mo^{VI}O_2(solv)]^{2+}$, where L^+ represents the oxidized form of Mo-coordinating phenol−thiosemicarbazone ligand. This proposed step of the photoredox cycle is supported by both the visible spectra obtained shortly after irradiation and the irreversible oxidation wave in the cyclic voltammogram of the dyad. As a consequence, back electron transfer from $MV^{\bullet+}$ to Ru^{III} is outcompeted. The presence of $MV^{\bullet+}$ is clearly seen in Sample C, in which the deep blue-green color of $MV^{\bullet+}$ persists, since the catalytic OAT cycle cannot turn over in the absence of molybdenum.

Scheme 3. Proposed Catalytic Mechanism That Combines Photoredox Catalysis Involving Single Electron Transfer (SET) with Oxygen Atom Transfer (OAT)

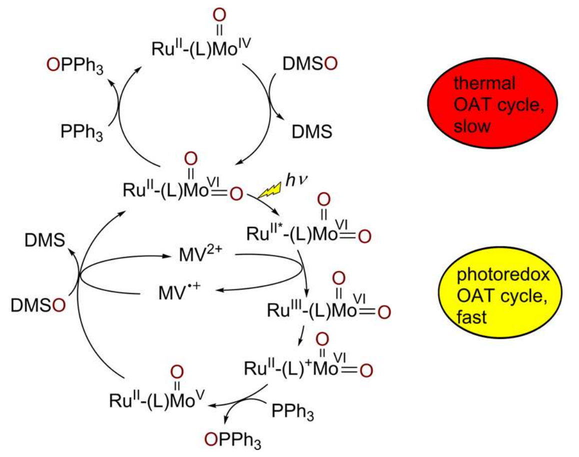

In the presence of molybdenum (sample A), the subsequent OAT to PPh_3 gives $OPPh_3$, which was detected by NMR spectroscopy, and a species with an electronic absorption spectrum that closely resembles that obtained for the species generated by electrochemical reduction, tentatively assigned as $[Ru^{II}(bpy)_2(\mathbf{L^2})Mo^{V}O(solv)]^{2+}$. The reductive half-reaction with DMSO produces DMS and regenerates MV^{2+} and Ru^{II}-(L)$Mo^{VI}(O)_2$. While in-depth investigations are required to determine the exact mechanistic and kinetics details, in particular, of the reductive half-reaction, our tests show that the photoactivated OAT cycle runs significantly faster than the thermal OAT cycle, which proceeds in the absence of light.

CONCLUSIONS

The Ru(II)–Mo(VI) dyad $[Ru(bpy)_2(\mathbf{L^2})MoO_2(solv)]^{2+}$ was synthesized, fully characterized, and shown to accelerate the rate-determining step in the *cis*-dioxo molybdenum-catalyzed OAT cycle, the transfer of an oxo ligand to PPh_3, via a photoredox process. The energy provided by visible light is sufficient to generate a highly reactive, oxidized form of the molybdenum-centered catalyst, in which the noninnocent phenol–thiosemicarbazone ligand plays key role. The single electron transfer (SET) step in the photoredox process is essential in making the reactive one-electron oxidized form of the thiosemicarbazone complex accessible. In contrast, electrochemical methods trigger an irreversible two-electron oxidation process. Methylviologen acts as a mediator in the photoredox cycle, but it is regenerated and hence only required in catalytic rather than sacrificial amounts. By combining the ruthenium-polypyridyl-based photoredox cycle with the molybdenum-catalyzed OAT cycle, the rate acceleration of the OAT can be switched on and off via the light source.

The dyad can be regarded as an advanced bioinspired model for Mo-containing oxotransferases, since it demonstrates the importance of both spatially separated one-electron transfer units and the participation of a noninnocent S-containing ligand in OAT catalysis.

Interestingly, significant rate enhancement was also observed when two separate sensitizer and catalyst components were tested. Even though the effect seen with the bimolecular system was less pronounced than that observed with the covalently linked dyad, the reduced synthetic effort allows for the testing of different catalyst-sensitizer combinations and a higher-throughput approach could facilitate the discovery and optimization of new photoredox-catalytic systems in the future.

ASSOCIATED CONTENT

Ⓢ Supporting Information

The Supporting Information is available free of charge on the ACS Publications website at DOI: 10.1021/acs.inorgchem.6b01485.

> CVs of $[Ru(bpy)_3]Cl_2$, $[MoO_2(\mathbf{L^{Me}})(solv)]$, H_2-$\mathbf{L^{Me}}$, and methyl viologen dichloride; spectro-electrochemical information provided by control compounds; photograph of samples A–E before irradiation; EPR simulation parameters, ^1H and ^{31}P NMR spectra recorded after irradiation for samples A, C, D, and E; NMR spectra and mass spectra of synthesized compounds. (PDF)

AUTHOR INFORMATION

Corresponding Author

*E-mail: anne.duhme-klair@york.ac.uk.

Funding

EPSRC (EP/J019666/1), COST Action CM1003.

Notes

The authors declare no competing financial interest.

Experimental data sets associated with this paper were deposited with the Univ. of York library (www.york.ac.uk/library/info-for/researchers/datasets/).

ACKNOWLEDGMENTS

We thank the EPSRC (EP/J019666/1), COST Action CM1003 (Biological oxidation reactions—mechanisms and design of new catalysts) and the Univ. of York for financial support and Drs. A. Parkin and V. Chechik for helpful discussions. Experimental support provided by K. Heaton (mass spectrometry), H. Fish (NMR), and P. Groves (EPR) is gratefully acknowledged.

REFERENCES

(1) Harel, A.; Bromberg, Y.; Falkowski, P. G.; Bhattacharya, D. Evolutionary history of redox metal-binding domains across the tree of life. *Proc. Natl. Acad. Sci. U. S. A.* **2014**, *111*, 7042–7047.

(2) Holm, R. H.; Donahue, J. P. A thermodynamic scale for oxygen atom transfer reactions. *Polyhedron* **1993**, *12*, 571–589.

(3) Dempsey, J. L.; Winkler, J. R.; Gray, H. B. Proton-coupled electron flow in protein redox machines. *Chem. Rev.* **2010**, *110*, 7024–7039.

(4) Warren, J. J.; Mayer, J. M. Moving protons and electrons in biomimetic systems. *Biochemistry* **2015**, *54*, 1863–1878.

(5) Ghosh, S.; Hogarth, G.; Hollingsworth, N.; Holt, K. B.; Kabir, S. E.; Sanchez, B. E. Hydrogenase biomimetics: $Fe_2(CO)_4(\mu$-dppf)(μ-pdt) (dppf = 1,1′-bis(diphenylphosphino)ferrocene) both a proton-reduction and hydrogen oxidation catalyst. *Chem. Commun.* **2014**, *50*, 945–947.

(6) Camara, J. M.; Rauchfuss, T. B. Combining acid-base, redox and substrate binding functionalities to give a complete model for the [FeFe]-hydrogenase. *Nat. Chem.* **2011**, *4*, 26–30.

(7) Hüttinger, K.; Förster, C.; Heinze, K. Intramolecular electron transfer between molybdenum and iron mimicking bacterial sulphite dehydrogenase. *Chem. Commun.* **2014**, *50*, 4285–4288.

(8) Whiteoak, C. J.; Britovsek, G. J. P.; Gibson, V. C.; White, A. J. P. Electronic effects in oxo transfer reactions catalyzed by salan molybdenum(VI) *cis*-dioxo complexes. *Dalton Trans.* **2009**, 2337–2344.

(9) Herrero, C.; Quaranta, A.; Leibl, W.; Rutherford, A. W.; Aukauloo, A. Artificial photosynthetic systems. Using light and water to provide electrons and protons for the synthesis of a fuel. *Energy Environ. Sci.* **2011**, *4*, 2353–2365.

(10) Ott, S.; Borgström, M.; Kritikos, M.; Lomoth, R.; Bergquist, J.; Akermark, B.; Hammarström, L.; Sun, L. Model of the iron hydrogenase active site covalently linked to a ruthenium photosensitizer: synthesis and photophysical properties. *Inorg. Chem.* **2004**, *43*, 4683–4692.

(11) Summers, P. A.; Calladine, J. A.; Ghiotto, F.; Dawson, J.; Sun, S.-Z.; Hamilton, M. L.; Towrie, M.; Davies, E. S.; McMaster, J.; George, M. W.; Schröder, M. Synthesis and photophysical study of a [NiFe] hydrogenase biomimetic compound covalently linked to a Re-diimine photosensitizer. *Inorg. Chem.* **2016**, *55*, 527–536.

(12) Prier, C. K.; Rankic, D. A.; MacMillan, D. W. C. Visible light photoredox catalysis with transition metal complexes: applications in organic synthesis. *Chem. Rev.* **2013**, *113*, 5322–5363.

(13) Angnes, R. A.; Li, Z.; Correia, C. R. D.; Hammond, G. B. Recent synthetic additions to the visible light photoredox toolbox. *Org. Biomol. Chem.* **2015**, *13*, 9152–9167.

(14) Lang, X.; Zhao, J.; Chen, X. Cooperative photoredox catalysis. *Chem. Soc. Rev.* **2016**, *45*, 3026–3038.

(15) Iali, W.; Lanoe, P.-H.; Torelli, S.; Jouvenot, D.; Loiseau, F.; Lebrun, C.; Hamelin, O.; Ménage, S. A ruthenium(II)-copper(II) dyad for the photocatalytic oxygenation of organic substrates mediated by dioxygen activation. *Angew. Chem., Int. Ed.* **2015**, *54*, 8415–8419.

(16) Herrero, C.; Quaranta, A.; Sircoglou, M.; Sénéchal-David, K.; Baron, A.; Marín, I. M.; Buron, C.; Baltaze, J.-P.; Leibl, W.; Aukauloo, A.; Banse, F. Successive light-induced two electron transfers in a Ru-Fe supramolecular assembly: from Fu-Fe(II)-OH_2 to Ru-Fe(IV)-oxo. *Chem. Sci.* **2015**, *6*, 2323–2327.

(17) Hille, R. The mononuclear molybdenum enzymes. *Chem. Rev.* **1996**, *96*, 2757–2816.

(18) Basu, P.; Raitsimring, A. M.; LaBarre, M. J.; Dhawan, I. K.; Weibrecht, J. L.; Enemark, J. H. Covalently linked oxomolybdenum-(V) and iron(III) porphyrin centers: Synthetic models for the

molybdenum-iron interaction in sulfite oxidase. *J. Am. Chem. Soc.* **1994**, *116*, 7166−7176.

(19) Wall, M. H.; Basu, P.; Buranda, T.; Wicks, B. S.; Findsen, E. W.; Ondrias, M.; Enemark, J. H.; Kirk, M. L. Potoinduced electron transfer in covalently linked oxomolybdenum(V) porphyrin systems. *Inorg. Chem.* **1997**, *36*, 5676−5677.

(20) Heinze, K. Bioinspired functional analogs of the active site of molybdenum enzymes: Intermediates and mechanisms. *Coord. Chem. Rev.* **2015**, *300*, 121−141.

(21) Holm, R. H. Metal-centered oxygen atom transfer reactions. *Chem. Rev.* **1987**, *87*, 1401−1449.

(22) Enemark, J. H.; Cooney, J. J. A.; Wang, J.-J.; Holm, R. H. Synthetic analogues and reaction systems relevant to the molybdenum and tungsten oxotransferases. *Chem. Rev.* **2004**, *104*, 1175−1200.

(23) Sugimoto, H.; Tsukube, H. Chemical analogues relevant to molybdenum and tungsten enzyme reaction centres toward structural dynamics and reaction diversity. *Chem. Soc. Rev.* **2008**, *37*, 2609−2619.

(24) Schulzke, C. Molybdenum and tungsten oxidoreductase models. *Eur. J. Inorg. Chem.* **2011**, *2011*, 1189−1199.

(25) Lobana, T. S.; Sharma, R.; Bawa, G.; Khanna, S. Bonding and structure trends of thiosemicarbazone derivatives of metals - An overview. *Coord. Chem. Rev.* **2009**, *253*, 977−1055.

(26) Stelzig, L.; Kötte, S.; Krebs, B. Molybdenum complexes with tridentate NS_2 ligands. Synthesis, crystal structures and spectroscopic properties. *J. Chem. Soc., Dalton Trans.* **1998**, 2921−2926.

(27) Eierhoff, D.; Tung, W. C.; Hammerschmidt, A.; Krebs, B. Molybdenum complexes with tridentate NS_2 ligands. Synthesis, crystal structures and spectroscopic properties. *Inorg. Chim. Acta* **2009**, *362*, 915−928.

(28) Ducrot, A.; Scattergood, B.; Coulson, B.; Perutz, R. N.; Duhme-Klair, A.-K. Electronic fine-tuning of oxygen atom transfer reactivity of *cis*-dioxomolybdenum(VI) complexes with thiosemicarbazone ligands. *Eur. J. Inorg. Chem.* **2015**, *2015*, 3562−3571.

(29) Pietsch, M. A.; Hall, M. B. Theoretical studies on models for the oxo-transfer reaction of dioxomolybdenum enzymes. *Inorg. Chem.* **1996**, *35*, 1273−1278.

(30) Kail, B. W.; Perez, L. M.; Zaric, S.; Millar, A. J.; Young, C. G.; Hall, M. B.; Basu, P. Mechanistic investigation of the oxygen-atom-transfer reactivity of dioxo-molybdenum(VI) complexes. *Chem. - Eur. J.* **2006**, *12*, 7501−7509.

(31) Gehrke, H.; Veal, J. Acetylacetonate complexes of molybdenum-(V) and molybdenum(VI). I. *Inorg. Chim. Acta* **1969**, *3*, 623−627.

(32) Bagherzadeh, M.; Zare, M. Synthesis, characterization, and catalysis of recyclable new piperazine-bridged Mo(VI) polymers $[MoO_2(Salen)\ (piperazine)]_n$ in highly selective oxygenation of alkenes and sulphides. *J. Coord. Chem.* **2013**, *66*, 2885−2900.

(33) Ellis, C. D.; Margerum, L. D.; Murray, R. W.; Meyer, T. J. Oxidative electropolymerisation of polypyridyl complexes of ruthenium. *Inorg. Chem.* **1983**, *22*, 1283−1291.

(34) Suzuki, K.; Kobayashi, A.; Kaneko, S.; Takehira, K.; Yoshihara, T.; Ishida, H.; Shiina, Y.; Oishi, S.; Tobita, S. Reevaluation of absolute luminescence quantum yields of standard solutions using a spectrometer with an integrating sphere and a back-thinned CCD detector. *Phys. Chem. Chem. Phys.* **2009**, *11*, 9850−9860.

(35) Purohit, S.; Koley, A. P.; Prasad, L. S.; Manoharan, P. T.; Ghosh, S. Chemistry of molybdenum with hard-soft donor ligands. 2. Molybdenum(VI), -(V), and − (IV) oxo complexes with tridentate Schiff base ligands. *Inorg. Chem.* **1989**, *28*, 3735−3742.

(36) Staniewicz, R. J.; Sympson, R. F.; Hendricker, D. G. Preparation and investigation of the spectral and electrochemical properties of mixed-ligand ruthenium(II) complexes containing 1,8-naphthyridines. *Inorg. Chem.* **1977**, *16*, 2166−2171.

(37) Stark, C. W.; Schreier, W. J.; Lucon, J.; Edwards, E.; Douglas, T.; Kohler, B. Interligand electron transfer in heteroleptic ruthenium(II) complexes occurs on multiple time scales. *J. Phys. Chem. A* **2015**, *119*, 4813−4824.

(38) Magde, D.; Magde, M. D., Jr.; Glazer, E. C. So-called "dual emission" for ^{3}MLCT luminescence in ruthenium complex ions: What is really happening? *Coord. Chem. Rev.* **2016**, *306*, 447−467.

(39) Zhang, M.-T.; Irebo, T.; Johansson, O.; Hammarström, L. Proton-coupled electron transfer from tyrosine: A strong rate dependence of intramolecular proton transfer distance. *J. Am. Chem. Soc.* **2011**, *133*, 13224−13227.

(40) Duman, S.; Kizilcikli, I.; Koca, A.; Akkurt, M.; Ülküseven, B. ONN-complexes of dioxomolybdenum(VI) with 2-hydroxy-1-naphthaldehyde S-ethyl-4-H/phenyl-thiosemicarbazones: Crystal structure, electrochemistry and *in situ* spectroelectrochemistry. *Polyhedron* **2010**, *29*, 2924−2932.

(41) Mondal, J. U.; Zamora, J. G.; Kinon, M. D.; Schultz, F. A. Six-coordinate monooxo molybdenum(VI) complexes with catecholate and salicylaldehyde thiosemicarbazone ligands. *Inorg. Chim. Acta* **2000**, *309*, 147−150.

(42) Pedrido, R.; Romero, M. J.; Bermejo, M. R.; González-Noya, A. M.; García-Lema, I.; Zaragoza, G. Metal-catalyzed oxidation processes in thiosemicarbazones: New complexes with the ligand *N*-{2-([4-*N*-ethylthiosemicarbazone]-methyl)phenyl}-*p*-toluenesulfonamide. *Chem. - Eur. J.* **2008**, *14*, 500−512.

(43) Lomoth, R.; Häupl, T.; Johansson, O.; Hammarström, L. Redox-switchable direction of photoinduced electron transfer in an $Ru(bpy)_3^{2+}$-viologen dyad. *Chem. - Eur. J.* **2002**, *8*, 102−110.

(44) Dunham, W. R.; Fee, J. A.; Harding, L. J.; Grande, H. J. Application of fast Fourier transforms to EPR spectra of free radicals in solution. *J. Magn. Reson.* **1980**, *40*, 351−359.